GSA Data Repository 2018076

Deccan volcanism caused coupled pCO_2 and terrestrial temperature rises, and pre-impact extinctions in North China

Authors: Laiming Zhang, Chengshan Wang, Paul B. Wignall, Tobias Kluge, Xiaoqiao Wan, Qian Wang, Yuan Gao

This Data Repository entry contains:

- Supplementary Information
  - Geological Background
    - Stratigraphy
    - Age model
  - Materials and Methods
    - Sample collection
    - Sample preparation

- Sample preservation style
- Clumped isotope analyses
- Calculation of average stable and clumped isotope values
- Δ_{47}-Temperature calibrations
- Calculation of paleo-atmospheric CO_2 concentrations

- Supplementary References
- Supplementary Figures
  - Figure DR1 Schematic paleogeography map
  - Figure DR2 Age model
  - Figure DR3 Petrographic images
  - Figure DR4 The results of stable and clumped isotopes analyses
  - Figure DR5 The $\delta^{18}O_{water}$ values (soil water) vs Δ_{47} temperature
  - Figure DR6 A comparison between Δ_{47} temperature from the Songliao Basin and North America

- Figure DR7 A comparison between analyses of same samples from different labs

- Figure DR8 Fossil range data from the Songliao Basin across the K-Pg boundary interval

- Supplementary Tables

  - Table DR1 Raw clumped isotope data in Johns Hopkins University

  - Table DR2 Raw clumped isotope data in Heidelberg University

  - Table DR3 Raw data for pCO_2 record

  - Table DR4 Results of clumped isotope analyses.

  - Table DR5 A summary of climatic parameters.

Geological Background

Stratigraphy

The Songliao Basin is approximately 820 km long in a north-south direction and approximately 350 km wide in an east-west direction, and covers ~260,000 km^2 in NE China (Fig. 1). Paleomagnetic data indicate that Songliao Basin was located at mid-latitudes in the Cretaceous similar to where it is now (Wang et al., 2013a; Wang et al., 2013b) (Fig. DR1).

The basin is filled predominantly with volcaniclastic, alluvial fan, fluvial and lacustrine sediments of the Late Jurassic, Cretaceous and Paleogene ages (Wang et al., 2013a; Wang et al., 2013b). From the bottom to the top, the Mesozoic sedimentary cover within the basin are the Upper Jurassic Huoshiling Formation (J3h); the Lower Cretaceous Shahezi (K1sh), Yingcheng (K1y), Denglouku (K1d), and Quantou (K1q) formations; the Upper Cretaceous Qinshankou (K2qn), Yaojia (K2y), Nenjiang (K2n), Sifangtai (K2s), and Mingshui (K2m) formations (Wang et al., 2013a).

The Late Cretaceous stratigraphy was recovered in a borehole named SK-In (north core) (44°12′44.22″N, 124°15′56.78″E; Fig. 1 and DR1) in the central part of Songliao Basin by the “Cretaceous Continental Scientific Drilling Program of China” (Wang et al., 2013a; Wang et al., 2013b). A high-temporal-resolution age model (Fig. DR2) was established for the SK-In borehole using a geomagnetic polarity sequence, U-Pb zircon ages, Milankovitch cycles, and biostratigraphic data (He et al., 2012; Deng et al., 2013; Wan et al., 2013; Wu et al., 2014; Wang et al., 2016).

Diverse lines of evidences place the K-Pg boundary in the top part of the Mingshui Formation (Li et al., 2011; Deng et al., 2013; Wan et al., 2013). According to the magnetostratigraphy, the chron C29r was recorded at the depth interval of 317.03-342.1 m in the north borehole (Deng et al., 2013), which corresponds to the top part of the Mingshui Formation. In addition, biostratigraphic studies also indicate major micropaleontologic changes in the top part of the Mingshui Formation (Li et al., 2011; Wan et al., 2013). The Sifangtai and Mingshui formations are composed of gray-green, gray, black and brown-red shale and gray-green sandstone, and consists of alluvial plain - shore to shallow lake - alluvial plain deposits across most of the basin (Wang et al., 2013a). They record a semi-humid, temperate environment developed during the post-rift phase of the basin (Chamberlain et al., 2013; Wang et al., 2013a).

Age model

The chronology of SK-In borehole has been well established using a combination of biostratigraphy (Wan et al., 2013), magnetostratigraphy (Deng et al., 2013), cyclostratigraphy (Wu et al., 2014) and radiometric ages (He et al., 2012; Wang et al., 2016) (Fig. DR2). Eleven magnetozones with five reversed, five normal and one mixed polarities were identified in SK-In (Deng et al., 2013). The lowermost geomagnetic reversal is interpreted as the C34n/C33r boundary based on a SIMS U-Pb zircon age of 83.7 ± 0.8 Ma (He et al., 2012) and a CA-ID-TIMS U-Pb zircon age of 83.07 ± 0.15 Ma (Wang et al., 2016) obtained from below the lowermost geomagnetic reversal. In the Sifangtai and Mingshui formations, the following

magnetozones are present: the lower part of C29r (317.0-342.1m), C30n-C31n (342.1-530.78m), C31r (530.78-700.88 m), and C32n (700.88-852.6m), C32r.1r (852.6-887.8m), C32r.1n (887.8-895.8m), C32r.2r (895.8-910.2m), C33n (910.2-1020.4m).

The 405 kyr eccentricity cycles were recognized using thorium (Th) data from the Sifangtai and Mingshui formations (Wu et al., 2014). The C30n/C29r boundary is very close to a minimum in the 405-kyr eccentricity cycle and about 300-400 ky older than the K-Pg boundary (Husson et al., 2011; Batenburg et al., 2014; Clyde et al., 2016). In the Mingshui Formation, the C30n/C29r boundary (66.398 Ma) (Gradstein et al., 2012) was set as the initial age control point and the maximum of the first 405 kyr eccentricity cycle above C30n/C29r boundary was set as the starting point. Then the maxima of the filtered 405 kyr sedimentary cycles were tuned to the maxima of the target 405 kyr eccentricity curve filtered from La2010d to establish an astronomical time scale (ATS) (Wu et al., 2014).

It is important to note that although the upper boundary for C29r is not clearly represented in the core, with C29r being overlaid by a “mixed polarity” interval, this does not have any influences on the age model. The location of the upper boundary for C29r was not used to determine the age model. The age model was established based on the 405 kyr eccentricity cycles recognized using thorium (Th) data from the Sifangtai and Mingshui formations and location of the C30n/C29r boundary, which are clearly determined.

In the ATS, the age of the C30n/C29r boundary is ~66.30 ± 0.08 Ma and the K-Pg boundary is ~66.001 ± 0.014 Ma, which is consistent with the GTS2012 (66.398

66 Ma and 66.04 Ma, respectively) (Gradstein et al., 2012) and results from marine strata
67 (Husson et al., 2011; Batenburg et al., 2014). Recently, the CA-ID-TIMS U-Pb zircon
68 ages of Deccan Traps have suggested that the age of the C30n/C29r boundary is very
69 close to the base of the main Deccan phase at 66.288 ± 0.027 Ma and the age of K-Pg
70 boundary is 65.968 ± 0.085 Ma (Schoene et al., 2015). The high-precision $^{40}Ar/^{39}Ar$
71 data suggests the age of the C30n/C29r boundary is 66.38 ± 0.05 Ma and the age of
72 K-Pg boundary is 66.043 ± 0.086 Ma (Renne et al., 2013; Renne et al., 2015). The U-
73 Pb ages from CA-ID-TIMS analysis suggests the C30n/C29r boundary is 66.436 ±
74 0.039 Ma and the age of K-Pg boundary is 66.021 ± 0.081 Ma (Clyde et al., 2016).
75 Therefore, the age model (ATS) of SK-In is reasonable and valid, and the age of each
76 sample can be calculated (see supplementary Table DR4 “Depth and ATS ages in the
77 SK-In borehole” in ref 5). In this study, the ages of paleosol carbonates were set at the
78 burial depth of the paleosol surfaces, not the depths of the carbonate nodules
79 themselves.

80 Although an iridium anomaly has not been located in SK-In, there are several
81 locations proposed for the K-Pg boundary (Li et al., 2011; Deng et al., 2013; Wan et
82 al., 2013). Based on a major palynofloral change, Li et al. (2011) suggested that the
83 K-Pg boundary should be located above 360.6 m. Based on a magnetostratigraphic
84 study, Deng et al. (2013) suggested that the K-Pg boundary should be located between
85 342.1-317.0 m. Based on the compiled data of charophytes, palynology, and
86 magnetostratigraphy, Wan et al. (2013) suggested that the K-Pg boundary should be
87 located at 328 m.

In this study, the K-Pg boundary was determined based on the ATS with resolution better than 0.1 Ma (Wu et al., 2014). As we mentioned above, the C30n/C29r boundary is about 300-340 ky older than the K-Pg boundary (Husson et al., 2011; Batenburg et al., 2014). With the C30n/C29r boundary located at 342.1m ± 1.4 m in depth (Deng et al., 2013), the location of the K-Pg boundary is 318 ± 1.2 m in depth (Wu et al., 2014).

According to Wu et al. (2014), the sediment accumulation rate was ~0.1 m/ky. In previous paleontological studies, the samples for ostracode extraction were taken at ~1 m (10 ky) intervals (Qu, 2014), the samples for spores/pollen extraction were taken at ~15-25 m (150-250 ky) intervals where mudstones and siltstones dominate and ~5-10 m (50-100 ky) intervals in the varicoloured segments (Li et al., 2011), and the samples for charophyte extraction were taken at ~1 m (10 ky) intervals (Li, 2013).

Materials and Methods

Sample collection

In the Sifangtai and Mingshui formations, many distinctive calcareous paleosols, or “calcisols” according to the Mack et al. (1993) soil classification, were identified and consist of carbonate nodules, slickensides, mottled colors, and fossil root traces (Huang et al., 2013; Gao et al., 2015) (Fig. DR2). They are interbedded with fluvial, alluvial, and lacustrine sediments. Due to the dehydration and recrystallization of iron hydroxides, the majority of Bk horizons are red in color and a minority are gray in color (Huang et al., 2013). The diameters of paleosol carbonate nodules are between 0.1-3.0 cm.

Paleosols generally form within 2,000-30,000 years from sediment or rock exposed at the earth surface (Kraus, 1999). The morphology of the paleosol nodules (Gile et al., 1966) in SK-In indicates they belong to stage I-II: “few filaments or faint coatings/few to common nodules”, which form in 100s to 1000s of years according to U-series isochron dating of Quaternary examples (Candy et al., 2005). These paleosol carbonates therefore provide a relatively continuous climate record at the time of their formation with temporal resolution better than tens of millennia.

In this study, 51 paleosol carbonates were collected from 44 paleosol Bk horizons of SK-In (Table DR4 and Table DR5). The diameters of the samples range from 1.0 to 3.0 cm. The depths of carbonate nodules (soil depth) below the paleosol surfaces (cm) and the burial depths of paleosols (m) were recorded. In practice, the resolution of burial depth is at a meter scale. Almost all the samples were collected from ≥ 30 cm below the paleosol surface, thus minimizing effects from diurnal heating and evaporation (Quade et al., 2013).

Sample preparation

A total of 40-50 mg of carbonate powder was drilled from a polished surface of each paleosol nodule by a micro-drill or milled by mortar and pestle. Drill depth was no deeper than 2 mm to avoid drilling secondary carbonate. Carbonate powder from different drill holes was homogenized. Drilling using a micro mill or equivalent system can partially convert aragonite to calcite and may also alter the Δ_{47} (Staudigel and Swart, 2016). However, in this study, all the paleosol carbonates are calcite and

drilling rotation speed was set <1,500 rpm to minimize frictional heating and Δ_{47} alteration.

Sample preservation style

Under optical and cathodoluminescence (CL) microscope all the samples were found to be dominated by dense micrite (except for sample "SK-31") with sparry calcite constrained to the cracks (Fig. DR3). This fine-grained, homogenous texture indicates that samples are very likely unaltered. In addition, our $\delta^{18}O$ and $\delta^{13}C$ values are similar to published data indicating no significant alteration (Fig. DR4). An exception is sample "SK-31", a sandstone with sparry calcite cement (Fig. DR3), that is unlikely to have recorded the original climatic signal.

In addition to obvious diagentic alteration solid-state reordering of C-O bonds may occur without significant changes of the bulk isotopes and textures of the carbonate (Henkes et al., 2014). The Mingshui Formation is the uppermost strata in Mesozoic and the depth of Cenozoic strata is less than 1 km in this region (Wang et al., 2013a). Therefore, in this study, all of the samples have experienced a short history of burial at a shallow depth (<76 myr and <1 km), which is below the burial limit (100 °C for 10^6-10^8 year) for solid-state C-O bond reordering (Henkes et al., 2014). There is no apparent relationship between Δ_{47} temperatures and burial depths or soil depth (below the soil surface) for the soil nodules analyzed, and also a lack of correlation of $\delta^{18}O$ value and soil depth (Fig. DR4). In addition, an expected (although weak) negative relationship between $\delta^{13}C$ value and soil depth is observed

(Fig. DR4). The correlation between the $\delta^{18}O_{water}$ and Δ_{47} temperatures also does not show signs of closed-system alteration (Fig. DR5). This suggests that our results reflect primary conditions and that the samples have, at most, only been slightly influenced by burial diagenesis or solid-state C-O bond reordering (Passey and Henkes, 2012; Henkes et al., 2014).

Notably, our Δ_{47} temperatures in Songliao Basin are similar to Δ_{47} temperatures of fossil bivalves (Tobin et al., 2014) and paleosol carbonates (Snell et al., 2014) (Fig. DR6) from similar paleolatitudes across the K-Pg boundary interval in North America, which further support the reliability of our results.

Clumped isotope analyses

Clumped isotope thermometry of carbonates provides a means of reconstructing the growth temperatures of carbonate minerals by evaluating the extent to which ^{13}C and ^{18}O are chemically bound to one another (clumped) within the same carbonate ion group. The technique is based on a homogeneous isotope exchange equilibrium and thus constrains temperature independent of the isotopic composition of waters from which carbonates grew (Eiler, 2011).

The clumped isotope analyses were conducted at Johns Hopkins University in 2013 and 2014 (the lab has now moved to University of Michigan, Ann Arbor) following the methods described in Passey et al. (2010). The CO_2 was liberated from 10-15 mg carbonate powder in an acid bath containing 105% H_3PO_4 at 90 °C for 10 min, then purified and introduced to a Thermo Scientific MAT 253 mass spectrometer

using an automated system. We report Δ_{47} values relative to the "absolute reference frame (ARF)" by periodically analyzing aliquots of enriched/depleted CO_2 that were isotopically equilibrated at 30°C or heated to 1000°C (Dennis et al., 2011). We also analyzed carbonate standards, HAF Carrara, NBS-19, or 102-GC-AZ01, alongside samples to monitor system stability and precision. In the first session, the long-term averages are HAF Carrara (n = 10) Δ_{47} = 0.398 ± 0.020‰ and 102-GC-AZ01 (n = 10) Δ_{47} = 0.698 ± 0.014‰ (ARF, mean ± 1σ standard deviation). In the second session, the long-term averages are HAF Carrara (n = 5) Δ_{47} = 0.398 ± 0.005‰, NBS-19 (n=5) Δ_{47} = 0.405 ± 0.011‰, and 102-GC-AZ01 (n = 9) Δ_{47} = 0.695 ± 0.007‰ (ARF, mean ± 1σ standard deviation) (Table DR1). The long term accepted values are HAF Carrara Δ_{47} = 0.396‰, NBS-19 Δ_{47} = 0.393‰, and 102-GC-AZ01 Δ_{47} = 0.714‰. The observed long-term Standard Deviation (SD) of lab standards is 0.013‰. The ^{17}O correction was applied (Schauer et al., 2016) and the differences are within 0.01‰. The parameters in the original CIDS files were changed. According to Daëron et al. (2016), the R13 (VPDB) was changed from 0.0112372 to 0.011180, the R17 (VSMOW) changed from 0.0003799 to 0.00038475, and the λ value changed from 0.5164 to 0.528.

In 2017, further clumped isotope analyses were conducted at Heidelberg University following the methods described in Kluge et al. (2015). Between 6 to 8 mg of carbonate powder (equivalent to 2-3 mg pure carbonate powder) were reacted for 10 minutes in 105% phosphoric acid held at 90 °C. Then CO_2 gas was purified by passage through a conventional off-line vacuum line with multiple cryogenic traps

and a Porapak-Q trap held at -35 °C. The purified CO_2 gas was analyzed using a MAT 253 Plus mass spectrometer from Thermo Fisher Scientific equipped with 10^{13} ohm resistors at masses 47-49 and includes a background monitoring cup. The data are reported relative to the "absolute reference frame (ARF)" by periodically analyzing gas standards that were isotopically equilibrated at 5°C and 90°C or heated to 1000°C (Dennis et al., 2011) and compared with calcite standards, Marble Richter, ETH-1, ETH-2, ETH-3, ETH-4, H-II, and L, alongside samples. The average values (ARF, mean ± 1σ standard deviation) for the measurement period is 0.292 ± 0.015‰ (n = 3) for ETH-1, 0.305 ± 0.006‰ (n = 3) for ETH-2, 0.712 ± 0.014‰ (n = 6) for H-II and L, and 0.396 ± 0.019‰ (n = 3) for Marble Richter. The observed long-term Standard Deviation (SD) of lab standards is 0.013‰. The ^{17}O correction was applied as described above (Schauer et al., 2016).

The Δ_{47} temperatures are calculated using the calibration of Passey and Henkes (2012) with an acid temperature correction of 0.082% (Defliese et al., 2015). The $\delta^{18}O_{water}$ (soil water) are calculated from the Δ_{47} temperatures and $\delta^{18}O$ of paleosol carbonates using the calibration of Kim and O'Neil (1997). The $\delta^{13}C$ and $\delta^{18}O$ are reported relative to either the VPDB (mineral) or the VSMOW (water) scales (Table DR1 and DR2). Four samples were analyzed in both labs to evaluate the possible differences from the slightly different methods and machines used in Johns Hopkins and Heidelberg. This showed only very small differences in the $\delta^{13}C$, the $\delta^{18}O$, the Δ_{47}, and the $\delta^{18}O_{water}$ values (Fig. DR7), and therefore would not have any effect on the interpretations of the results.

220

221 Calculation of average stable and clumped isotope values

222 Average $\delta^{13}C$ and $\delta^{18}O$ values are calculated as the mean of n (2-3) replicates
223 with error taken as 1 standard deviation (SD). Average Δ_{47} values are calculated as the
224 mean of n (2-3) replicates with error taken as 1 standard error (SE) (Table DR4). The
225 SE of Δ_{47} equal to SD divided by the square root of n (2-3). When SD of a sample is
226 less than the observed long-term SD of lab standards (0.013‰), 0.013‰ is assigned
227 as the SD of the sample. Then the Δ_{47} temperatures and $\delta^{18}O_{water}$ values are calculated
228 from average Δ_{47} values and average $\delta^{18}O$ values. The 1 SE of Δ_{47} temperatures and
229 $\delta^{18}O_{water}$ values are calculated by Gaussian error propagation. For most samples, the
230 uncertainties are relatively consistent, generally lower than 5 °C. The relatively large
231 uncertainties may be due to the heterogeneity of the samples. We did notice a gradual
232 increase in the uncertainties. In this study, the uncertainties of Δ_{47} temperatures are
233 calculated by Gaussian error propagation and the Δ_{47} values are part of the
234 denominator in the equation. According to the equation, the relatively lower Δ_{47}
235 values (higher temperatures) for older (Campanian) samples would lead to a higher
236 uncertainty. Finally, the Δ_{47} temperatures of samples from the same burial depth are
237 averaged and treated equally, using the equation as the inverse variance weighted
238 mean (Table DR4 and Table DR5).

239

240 Δ_{47}-Temperature calibrations

Different Δ_{47}-temperature calibrations possess slightly different slopes and intercepts, which produces different results. Four of them are evaluated here (Table DR1 and DR2), these are calibrations from Passey and Henkes (2012), Defliese et al. (2015), Kluge et al. (2015), and Kelson et al. (2017).The acid temperature correction of 0.082‰ was adopted from Defliese et al. (2015).

The temperature curves generated by these calibrations show similar trends but with slightly different amplitudes (no more than 5 °C). The calibration of Passey and Henkes (2012) with an acid temperature correction of 0.082% (Defliese et al., 2015) was used. The controversies regarding Δ_{47}-temperature calibrations are of minor importance for this study as almost all calibrations produce values that overlap in the investigated temperature interval (Kluge et al., 2015).

Calculation of paleo-atmospheric CO_2 concentrations

The carbon isotopes of paleosol carbonate is mainly derived from two different $\delta^{13}C$ sources, the atmospheric CO_2 and the soil-respired CO_2. Therefore, the carbon isotope values of pedogenic carbonates will rise or fall alongside the variations of atmospheric CO_2 concentrations (Breecker and Retallack, 2014). The equations of paleo-atmospheric CO_2 concentration are:

$$P_a = P_r \times (\delta^{13}C_s - 1.0044\delta^{13}C_r - 4.4)/(\delta^{13}C_a - \delta^{13}C_s) \quad (1)$$

$$\delta^{13}C_s = (\delta^{13}C_c + 1000)/[(11.98 - 0.12T)/1000 + 1] - 1000 \quad (2)$$

$$\delta^{13}C_a = \delta^{13}C_{ocean} - 7.9 \quad (3)$$

$$\delta^{13}C_o = 1.1\delta^{13}C_a - 18.67 \quad (4)$$

$$\delta^{13}C_r = \delta^{13}C_o - 1 \quad (5)$$

$$P_r = 35.3D_s + 588 \quad (6)$$

$$D_s = D_p/[-0.62/(0.38/e^{0.17K} - 1)] \quad (7)$$

where P_a is the atmospheric CO_2 concentration (ppmv), P_r is the soil-respired CO_2 concentration (ppmv), and the $\delta^{13}C_s$, $\delta^{13}C_r$, and $\delta^{13}C_a$ are the stable carbon isotope compositions (‰) of soil CO_2, soil-respired CO_2, and the atmospheric CO_2, respectively. K (km) is the estimated thickness overburden of the samples (burial depth), and D_s/D_p (cm) are the original/buried soil depths carbonate nodules below the paleosol surfaces (Breecker and Retallack, 2014).

The $\delta^{13}C_s$ can be determined from the carbon isotope composition of the pedogenic carbonate ($\delta^{13}C_c$) and the formation temperature of the pedogenic carbonate (T: Δ_{47} temperature) using the "Eq. (2)". We estimated the $\delta^{13}C_a$ through the average δ^{13}C values of planktonic foraminifera ($\delta^{13}C_{ocean}$) (Thibault et al., 2012), and -7.9‰ was assumed as the isotopic equilibrium fractionation value between the

285 ocean and the atmospheric CO_2 (Passey and Cerling, 2002). The $\delta^{13}C_r$ can be
286 calculated from the organic matter ($\delta^{13}C_o$) in the paleosol (Breecker and Retallack,
287 2014), and the $\delta^{13}C_o$ in turn can be estimated from the $\delta^{13}C_a$. The standard errors of
288 the atmospheric CO_2 concentration (P_a) are calculated using the Gaussian error
289 propagation (Table DR3). The equations are those of Breecker and Retallack (2014).

Supplementary references:

Batenburg, S. J., Gale, A. S., Sprovieri, M., Hilgen, F. J., Thibault, N., Boussaha, M., and Orue-Etxebarria, X., 2014, An astronomical time scale for the Maastrichtian based on the Zumaia and Sopelana sections (Basque country, northern Spain): Journal of the Geological Society, v. 171, no. 2, p. 165-180.

Breecker, D. O., and Retallack, G. J., 2014, Refining the pedogenic carbonate atmospheric CO_2 proxy and application to Miocene CO_2: Palaeogeography, Palaeoclimatology, Palaeoecology, v. 406, p. 1-8.

Candy, I., Black, S., and Sellwood, B. W., 2005, U-series isochron dating of immature and mature calcretes as a basis for constructing Quaternary landform chronologies for the Sorbas basin, southeast Spain: Quaternary Research, v. 64, no. 1, p. 100-111.

Chamberlain, C. P., et al., 2013, Stable isotopic evidence for climate and basin evolution of the Late Cretaceous Songliao basin, China: Palaeogeography, Palaeoclimatology, Palaeoecology, v. 385, p. 106-124.

Clyde, W. C., Ramezani, J., Johnson, K. R., Bowring, S. A., and Jones, M. M., 2016, Direct high-precision U-Pb geochronology of the end-Cretaceous extinction and calibration of Paleocene astronomical timescales: Earth and Planetary Science Letters, v. 452, p. 272-280.

Daëron, M., Blamart, D., Peral, M., and Affek, H. P., 2016, Absolute isotopic abundance ratios and the accuracy of Δ47 measurements: Chemical Geology, v. 442, p. 83-96.

Defliese, W. F., Hren, M. T., and Lohmann, K. C., 2015, Compositional and temperature effects of phosphoric acid fractionation on Δ_{47} analysis and implications for discrepant calibrations: Chemical Geology, v. 396, p. 51-60.

312 Deng, C. L., He, H. Y., Pan, Y. X., and Zhu, R. X., 2013, Chronology of the terrestrial Upper
313 Cretaceous in the Songliao Basin, northeast Asia: Palaeogeography, Palaeoclimatology,
314 Palaeoecology, v. 385, p. 44-54.
315 Dennis, K. J., Affek, H. P., Passey, B. H., Schrag, D. P., and Eiler, J. M., 2011, Defining an absolute
316 reference frame for 'clumped' isotope studies of CO_2: Geochimica et Cosmochimica Acta, v.
317 75, no. 22, p. 7117-7131.
318 Eagle, R., et al., 2013, The influence of temperature and seawater carbonate saturation state on ^{13}C-^{18}O
319 bond ordering in bivalve mollusks: Biogeosciences Discuss, v. 10, p. 157-194.
320 Eiler, J. M., 2011, Paleoclimate reconstruction using carbonate clumped isotope thermometry:
321 Quaternary Science Reviews, v. 30, no. 25-26, p. 3575-3588.
322 Gao, Y., Ibarra, D. E., Wang, C., Caves, J. K., Chamberlain, C. P., Graham, S. A., and Wu, H., 2015,
323 Mid-latitude terrestrial climate of East Asia linked to global climate in the Late Cretaceous:
324 Geology, v. 43, no. 4, p. 287-290.
325 Ghosh, P., Adkins, J., Affek, H., Balta, B., Guo, W., Schauble, E. A., Schrag, D., and Eiler, J. M.,
326 2006, ^{13}C-^{18}O bonds in carbonate minerals: A new kind of paleothermometer: Geochimica et
327 Cosmochimica Acta, v. 70, no. 6, p. 1439-1456.
328 Gile, L. H., Peterson, F. F., and Grossman, R. B., 1966, Morphological and genetic sequences of
329 carbonate accumulation in desert soils: Soil Science, v. 101, no. 5, p. 347-360.
330 Gradstein, F. M., Ogg, G., and Schmitz, M., 2012, The Geologic Time Scale 2012 2-Volume Set,
331 Amsterdam, Elsevier.

He, H., Deng, C., Wang, P., Pan, Y., and Zhu, R., 2012, Toward age determination of the termination of the Cretaceous Normal Superchron: Geochemistry, Geophysics, Geosystems, v. 13, no. 2, p. Q02002.

Henkes, G. A., Passey, B. H., Grossman, E. L., Shenton, B. J., Pérez-Huerta, A., and Yancey, T. E., 2014, Temperature limits for preservation of primary calcite clumped isotope paleotemperatures: Geochimica et Cosmochimica Acta, v. 139, p. 362-382.

Henkes, G. A., Passey, B. H., Wanamaker Jr, A. D., Grossman, E. L., Ambrose Jr, W. G., and Carroll, M. L., 2013, Carbonate clumped isotope compositions of modern marine mollusk and brachiopod shells: Geochimica et Cosmochimica Acta, v. 106, p. 307-325.

Huang, C., Retallack, G. J., Wang, C., and Huang, Q., 2013, Paleoatmospheric pCO_2 fluctuations across the Cretaceous-Tertiary boundary recorded from paleosol carbonates in NE China: Palaeogeography, Palaeoclimatology, Palaeoecology, v. 385, p. 95-105.

Husson, D., Galbrun, B., Laskar, J., Hinnov, L. A., Thibault, N., Gardin, S., and Locklair, R. E., 2011, Astronomical calibration of the Maastrichtian (Late Cretaceous): Earth and Planetary Science Letters, v. 305, no. 3-4, p. 328-340.

Kelson, J. R., Huntington, K. W., Schauer, A. J., Saenger, C., and Lechler, A. R., 2017, Toward a universal carbonate clumped isotope calibration: Diverse synthesis and preparatory methods suggest a single temperature relationship: Geochimica et Cosmochimica Acta, v. 197, p. 104-131.

Kim, S.-T., and O'Neil, J. R., 1997, Equilibrium and nonequilibrium oxygen isotope effects in synthetic carbonates: Geochimica et Cosmochimica Acta, v. 61, no. 16, p. 3461-3475.

353 Kluge, T., John, C. M., Jourdan, A.-L., Davis, S., and Crawshaw, J., 2015, Laboratory calibration of
354 the calcium carbonate clumped isotope thermometer in the 25-250 °C temperature range:
355 Geochimica et Cosmochimica Acta, v. 157, p. 213-227.
356 Kraus, M. J., 1999, Paleosols in clastic sedimentary rocks: their geologic applications: Earth-Science
357 Reviews, v. 47, no. 1-2, p. 41-70.
358 Li, J., Batten, D. J., and Zhang, Y., 2011, Palynological record from a composite core through Late
359 Cretaceous-early Paleocene deposits in the Songliao Basin, Northeast China and its
360 biostratigraphic implications: Cretaceous Research, v. 32, no. 1, p. 1-12.
361 Li, S., 2012, Late Cretaceous-early Paleogene charophytes from Songliao Basin, North China: SK1
362 cores [Master thesis]: China University of Geosciences, Beijing, 64 p. (in Chinese with
363 English abstract)
364 Mack, G. H., James, W. C., and Monger, H. C., 1993, Classification of paleosols: Geological Society
365 of America Bulletin, v. 105, no. 2, p. 129-136.
366 Passey, B. H., and Cerling, T. E., 2002, Tooth enamel mineralization in ungulates: implications for
367 recovering a primary isotopic time-series: Geochimica et Cosmochimica Acta, v. 66, no. 18, p.
368 3225-3234.
369 Passey, B. H., and Henkes, G. A., 2012, Carbonate clumped isotope bond reordering and
370 geospeedometry: Earth and Planetary Science Letters, v. 351-352, p. 223-236.
371 Passey, B. H., Levin, N. E., Cerling, T. E., Brown, F. H., and Eiler, J. M., 2010, High-temperature
372 environments of human evolution in East Africa based on bond ordering in paleosol
373 carbonates: Proceedings of the National Academy of Sciences, v. 107, no. 25, p. 11245-
374 11249.

375 Qu, H., 2014, Late Cretaceous–early Paleocene ostracod biostratigraphy and the relationships between
376 the stable isotopic compositions of ostracod shells and the paleoenvironments in the Songliao
377 Basin, northeast China [Ph.D. thesis]: China University of Geosciences, Beijing, 128 p. (in
378 Chinese with English abstract)
379 Quade, J., Eiler, J., Daëron, M., and Achyuthan, H., 2013, The clumped isotope geothermometer in soil
380 and paleosol carbonate: Geochimica et Cosmochimica Acta, v. 105, p. 92-107.
381 Renne, P. R., Deino, A. L., Hilgen, F. J., Kuiper, K. F., Mark, D. F., Mitchell, W. S., Morgan, L. E.,
382 Mundil, R., and Smit, J., 2013, Time Scales of Critical Events Around the Cretaceous-
383 Paleogene Boundary: Science, v. 339, no. 6120, p. 684-687.
384 Renne, P. R., Sprain, C. J., Richards, M. A., Self, S., Vanderkluysen, L., and Pande, K., 2015, State
385 shift in Deccan volcanism at the Cretaceous-Paleogene boundary, possibly induced by impact:
386 Science, v. 350, no. 6256, p. 76-78.
387 Schauer, A. J., Kelson, J., Saenger, C., and Huntington, K. W., 2016, Choice of ^{17}O correction affects
388 clumped isotope (Δ_{47}) values of CO_2 measured with mass spectrometry: Rapid Commun Mass
389 Spectrom, v. 30, no. 24, p. 2607-2616.
390 Schoene, B., Samperton, K. M., Eddy, M. P., Keller, G., Adatte, T., Bowring, S. A., Khadri, S. F. R.,
391 and Gertsch, B., 2015, U-Pb geochronology of the Deccan Traps and relation to the end-
392 Cretaceous mass extinction: Science, v. 347, no. 6218, p. 182-184.
393 Scott, R. W., Wan, X., Wang, C., and Huang, Q., 2012, Late Cretaceous chronostratigraphy (Turonian-
394 Maastrichtian): SK1 core Songliao Basin, China: Geoscience Frontiers, v. 3, no. 4, p. 357-367.

395 Snell, K. E., Koch, P. L., Druschke, P., Foreman, B. Z., and Eiler, J. M., 2014, High elevation of the
396 'Nevadaplano' during the Late Cretaceous: Earth and Planetary Science Letters, v. 386, p. 52-
397 63.
398 Staudigel, P. T., and Swart, P. K., 2016, Isotopic behavior during the aragonite-calcite transition:
399 Implications for sample preparation and proxy interpretation: Chemical Geology, v. 442, p.
400 130-138.
401 Thibault, N., Husson, D., Harlou, R., Gardin, S., Galbrun, B., Huret, E., and Minoletti, F., 2012,
402 Astronomical calibration of upper Campanian–Maastrichtian carbon isotope events and
403 calcareous plankton biostratigraphy in the Indian Ocean (ODP Hole 762C): Implication for
404 the age of the Campanian–Maastrichtian boundary: Palaeogeography, Palaeoclimatology,
405 Palaeoecology, v. 337-338, p. 52-71.
406 Tobin, T. S., Ward, P. D., Steig, E. J., Olivero, E. B., Hilburn, I. A., Mitchell, R. N., Diamond, M. R.,
407 Raub, T. D., and Kirschvink, J. L., 2012, Extinction patterns, $\delta^{18}O$ trends, and
408 magnetostratigraphy from a southern high-latitude Cretaceous-Paleogene section: Links with
409 Deccan volcanism: Palaeogeography, Palaeoclimatology, Palaeoecology, v. 350-352, p. 180-
410 188.
411 Tobin, T. S., Wilson, G. P., Eiler, J. M., and Hartman, J. H., 2014, Environmental change across a
412 terrestrial Cretaceous-Paleogene boundary section in eastern Montana, USA, constrained by
413 carbonate clumped isotope paleothermometry: Geology, v. 42, no. 4, p. 351-354.
414 Wan, X., Zhao, J., Scott, R. W., Wang, P., Feng, Z., Huang, Q., and Xi, D., 2013, Late Cretaceous
415 stratigraphy, Songliao Basin, NE China: SK1 cores: Palaeogeography, Palaeoclimatology,
416 Palaeoecology, v. 385, p. 31-43.

417 Wang, C., Feng, Z., Zhang, L., Huang, Y., Cao, K., Wang, P., and Zhao, B., 2013a, Cretaceous
418 paleogeography and paleoclimate and the setting of SKI borehole sites in Songliao Basin,
419 northeast China: Palaeogeography, Palaeoclimatology, Palaeoecology, v. 385, p. 17-30.
420 Wang, C., Scott, R. W., Wan, X., Graham, S. A., Huang, Y., Wang, P., Wu, H., Dean, W. E., and
421 Zhang, L., 2013b, Late Cretaceous climate changes recorded in Eastern Asian lacustrine
422 deposits and North American Epieric sea strata: Earth-Science Reviews, v. 126, p. 275-299.
423 Wang, T., Ramezani, J., Wang, C., Wu, H., He, H., and Bowring, S. A., 2016, High-precision U-Pb
424 geochronologic constraints on the Late Cretaceous terrestrial cyclostratigraphy and
425 geomagnetic polarity from the Songliao Basin, Northeast China: Earth and Planetary Science
426 Letters, v. 446, p. 37-44.
427 Wilf, P., Johnson, K. R., and Huber, B. T., 2003, Correlated terrestrial and marine evidence for global
428 climate changes before mass extinction at the Cretaceous-Paleogene boundary: Proceedings of
429 the National Academy of Sciences, v. 100, no. 2, p. 599-604.
430 Wilson, G. P., DeMar, D. G., and Carter, G., 2014, Extinction and survival of salamander and
431 salamander-like amphibians across the Cretaceous-Paleogene boundary in northeastern
432 Montana, USA: Geological Society of America Special Papers, v. 503, p. 271-297.
433 Wu, H., Zhang, S., Hinnov, L. A., Jiang, G., Yang, T., Li, H., Wan, X., and Wang, C., 2014,
434 Cyclostratigraphy and orbital tuning of the terrestrial upper Santonian-Lower Danian in
435 Songliao Basin, northeastern China: Earth and Planetary Science Letters, v. 407, p. 82-95.

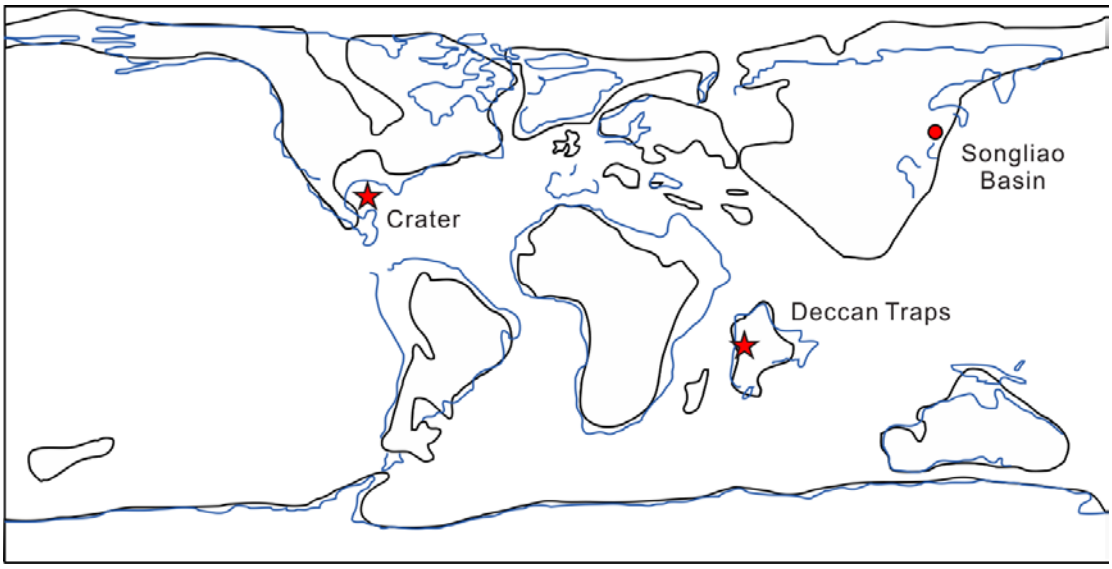

436

437 Fig. DR1. **Schematic paleogeography map.** Paleogeographic map of the K-Pg

438 boundary interval showing the locations of the Chicxulub impact crater, the Deccan

439 Traps, and the Songliao Basin (Wang et al., 2013a).

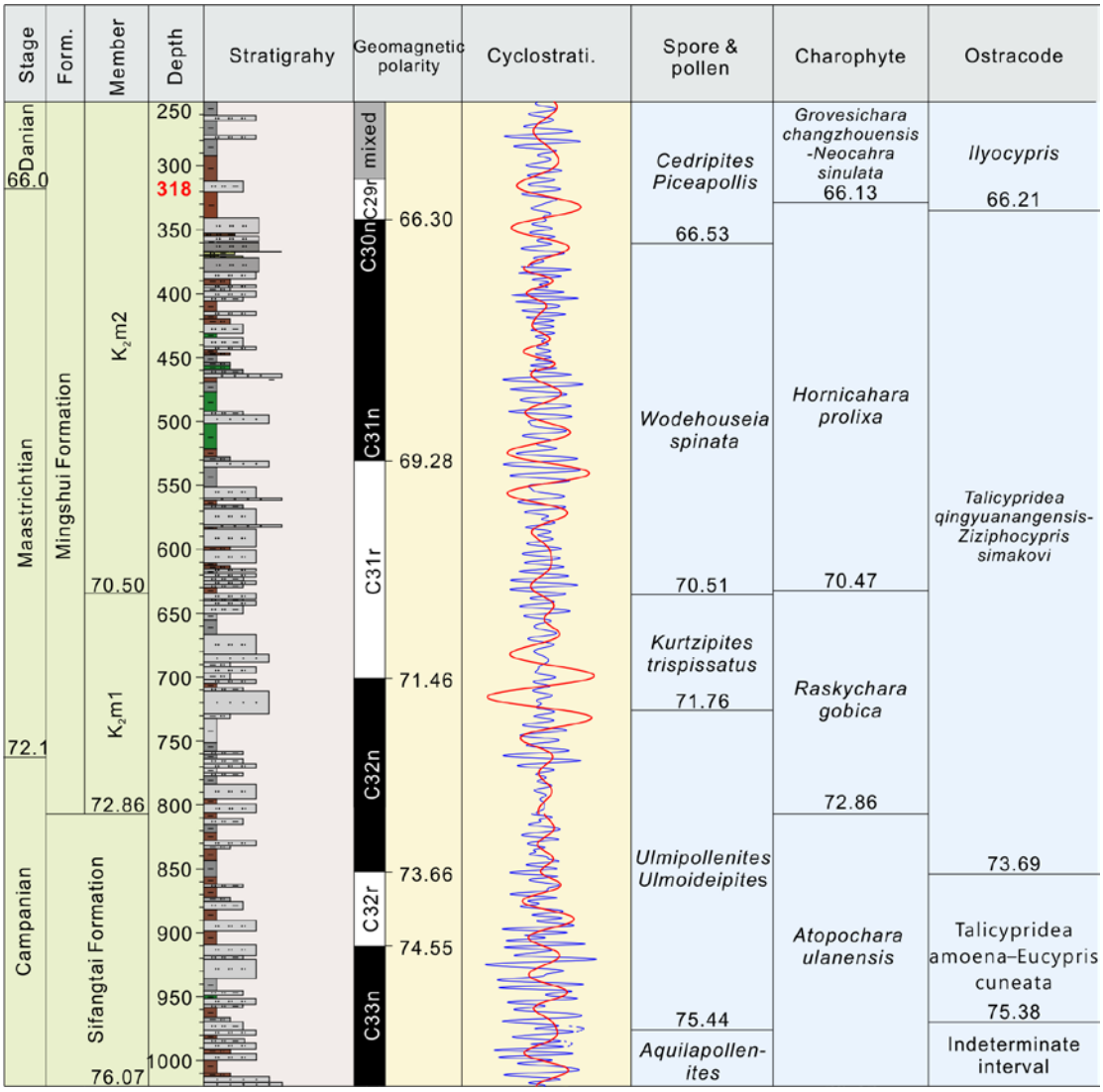

Fig. DR2. **Age model.** Integrated stratigraphic frame of the upper part of Sifangtai Formation and Mingshui Formation of the SK-In based on magnetostratigraphy (Deng et al., 2013), cyclostratigraphy (Wu et al., 2014), and biostratigraphy (Wan et al., 2013; Qu, 2014). The 405-kyr (red) and 100-kyr (blue) cycles are from Wu et al. (2014). The red bold number “318” in the “Depth” column represent the location of the K-Pg boundary. “Cyclostrati” represents “Cyclostratigraphy”. “Form.” represents “Formation”. Modified after Wan et al. (2013) and Wu et al. (2014).

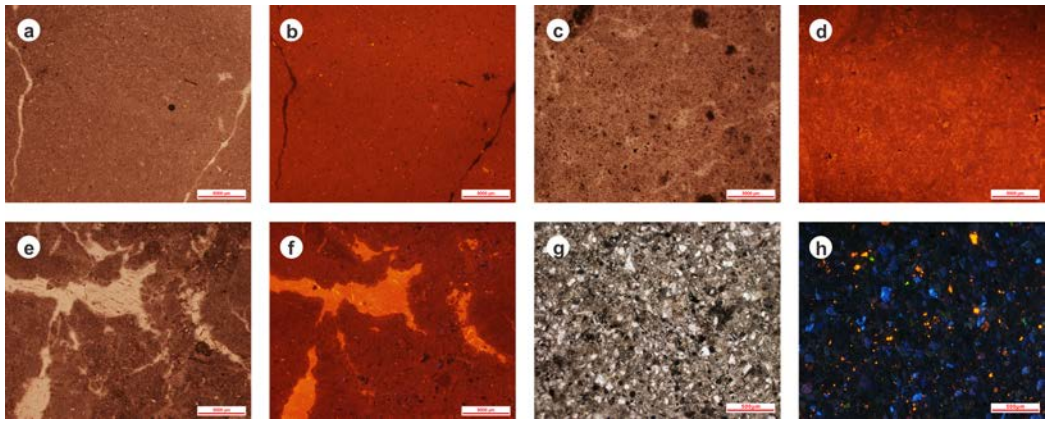

Fig. DR3. **Petrographic images.** (**a-d**) Optical and cathodoluminescence petrographic images for dense micrite. (**e-f**) Optical and cathodoluminescence petrographic images for dense micrite with fractures containing secondary spar. (**g-h**) Optical and cathodoluminescence petrographic images for the altered sample "SK-31".

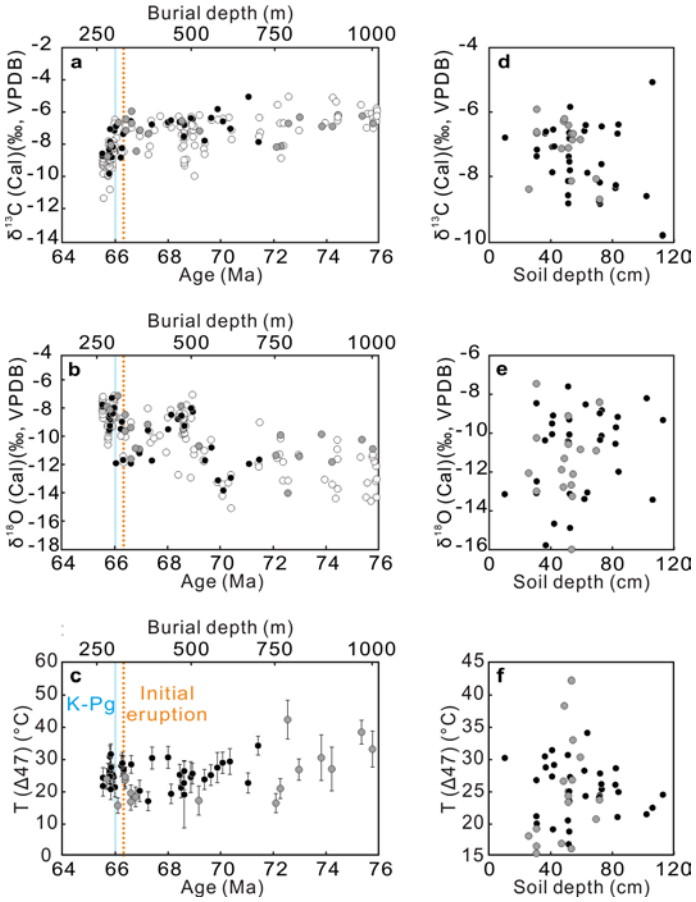

Fig. DR4. **The results of stable and clumped isotopes analyses.** (**a**) The $\delta^{13}C$ vs age/burial depth. (**b**) The $\delta^{18}O$ vs age/burial depth. (**c**) The Δ_{47} temperature vs age/burial depth. (**d**) The $\delta^{13}C$ vs soil depth. (**e**) The $\delta^{18}O$ vs soil depth. (**f**) The Δ_{47} temperature vs soil depth. The black (Johns Hopkins) and grey (Heidelberg) circles represent results of this study, and the white circles represent the previous published data from the Songliao Basin (Huang et al., 2013; Gao et al., 2015). The average 1σ standard error in $\delta^{13}C$ and $\delta^{18}O$ are < 0.07‰ and < 0.06‰, respectively. The 1σ standard error in the Δ_{47} temperatures are shown as vertical bars. The dotted orange line marks the onset of the main Deccan eruptions at 66.288 ± 0.085 Ma (Schoene et al., 2015) or 66.38 ± 0.05 Ma (Renne et al., 2015). The dotted blue line marks the K-Pg boundary at ~66.00 Ma (Wu et al., 2014) or 66.043 ± 0.086 Ma (Renne et al.,

2013) and the Chicxulub impact occurred at 66.038 Ma ± 0.098 Ma (Renne et al., 2013). The bulk and clumped isotope results for all the samples are presented in Table DR1, DR2, and DR4.

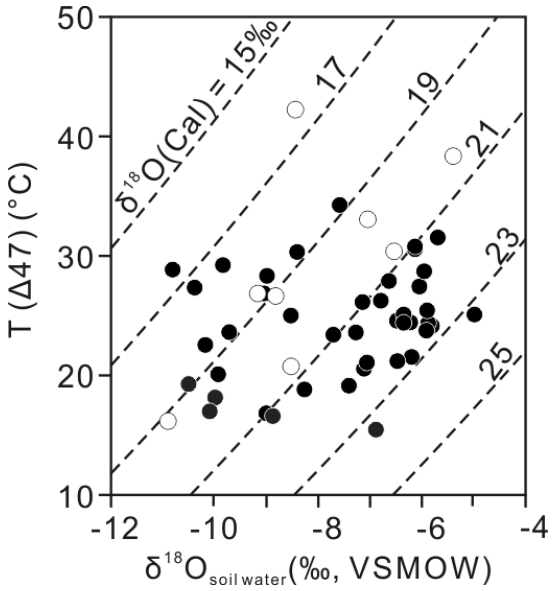

Fig. DR5. **The $\delta^{18}O_{water}$ values (soil water) vs Δ_{47} temperature.** Contours of $\delta^{18}O$ (Cal) (‰, VSMOW) calculated from the calibration Kim and O'Neil (1997). The black and white circles represent results from Maastrichtian and Campanian, respectively. There is no statistically correlation between Δ_{47} temperature and $\delta^{18}O_{water}$ values in the Maastrichtian, whereas in the Campanian there is a positive relationship.

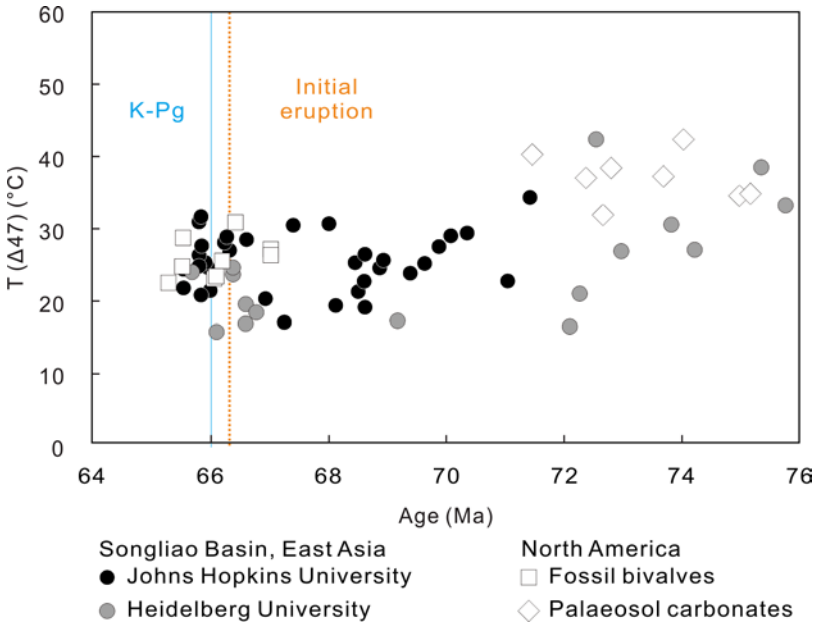

Fig. DR6. **A comparison between Δ_{47} temperature from the Songliao Basin and North America.** The black (Johns Hopkins) and gray (Heidelberg) circles represent Δ_{47} temperatures of paleosol carbonates in the Songliao Basin. The white squares and diamonds represent the Δ_{47} temperatures of fossil bivalves (Tobin et al., 2014) and paleosol carbonates (Snell et al., 2014) from similar paleolatitudes in North America (see legends).

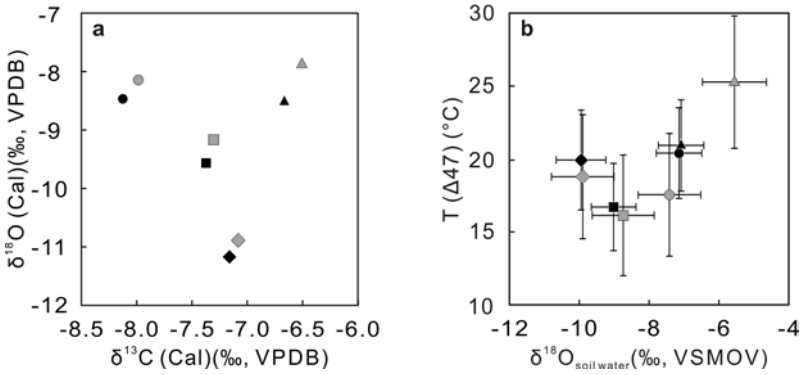

483

484 Fig. DR7. **A comparison between analyses of same samples from different labs.**

485 (**a**) The $\delta^{13}C$ vs $\delta^{18}O$. (**b**) The Δ_{47} temperature vs the $\delta^{18}O_{water}$ values. The 1σ standard

486 errors are shown as vertical/horizontal bars.

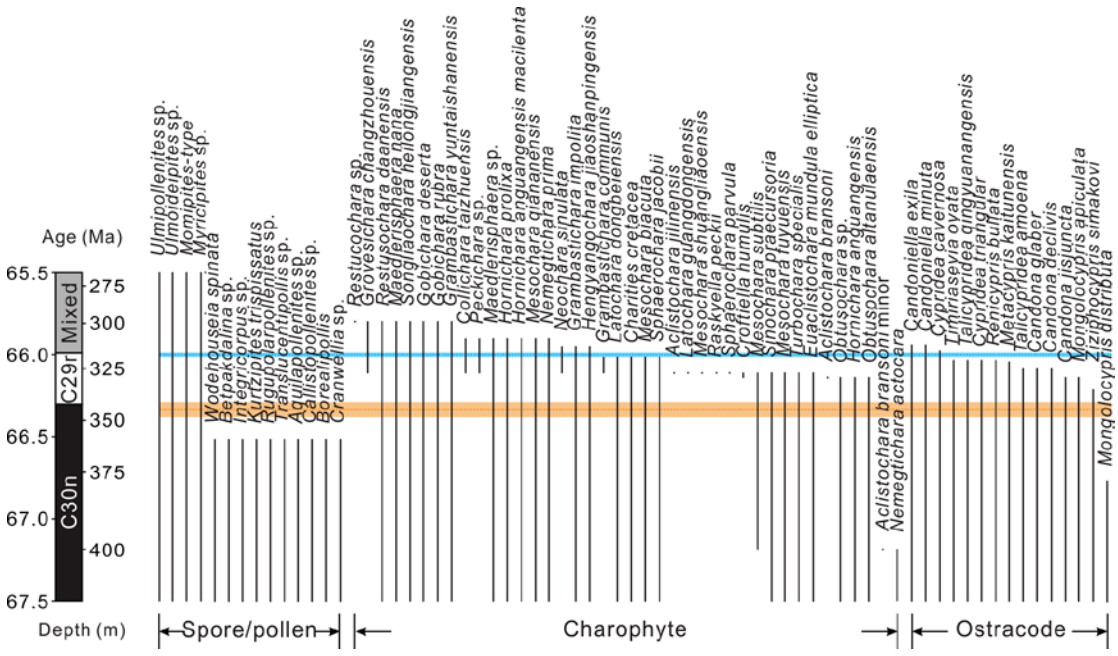

Fig. DR8. **Fossil range data from the Songliao Basin across the K-Pg boundary interval.** The fossil range data from the Songliao Basin is from Scott et al. (2012). The dotted orange line marks the onset of the main Deccan eruptions at 66.288 ± 0.085 Ma (Schoene et al., 2015) or 66.38 Ma ± 0.05 (Renne et al., 2015). The magnetozones are derived from Deng et al. (2013) and Wu et al. (2014). The dotted blue line marks the K-Pg boundary at ~66.00 Ma (Wu et al., 2014) or 66.043 ± 0.086 Ma (Renne et al., 2013) and the Chicxulub impact occurred at 66.038 Ma ± 0.098 Ma (Renne et al., 2013).

Table DR4 Results of clumped isotope analyses.

Sample ID	Age* (Ma)	Dp† (cm)	Burial depth (km)	Ds† (cm)	N‡	$\delta^{13}C$§ (‰, VPDB)	$\delta^{18}O$§ (‰, VPDB)	Δ47¶ (‰, ARF)	T(Δ47)‖ (°C)	$\delta^{18}O_{water}$** (‰, VSMOW)
SK-01	65.52	70	0.269	72	2	-8.75	-7.91	0.694 (0.009)	23.9 (3.2)	-5.8 (0.66)
SK-03	65.52	100	0.269	103	2	-8.59	-7.76	0.702 (0.009)	21.3 (3.2)	-6.2 (0.65)
SK-06	65.78	80	0.297	82	2	-8.35	-9.64	0.688 (0.009)	25.9 (3.3)	-7.1 (0.66)
SK-07	65.78	110	0.297	113	2	-9.80	-8.66	0.693 (0.009)	24.4 (3.3)	-6.5 (0.66)
SK-08	65.79	50	0.298	52	2	-8.57	-9.54	0.675 (0.009)	30.6 (3.5)	-6.1 (0.67)
SK-09	65.81	40	0.300	41	3	-7.85	-9.25	0.673 (0.010)	31.3 (3.9)	-5.7 (0.76)
SK-10	65.81	50	0.300	52	2	-8.12	-8.48	0.705 (0.009)	20.4 (3.1)	-7.1 (0.65)
SK-11	65.82	40	0.301	41	2	-7.07	-8.81	0.684 (0.009)	27.2 (3.3)	-6.0 (0.67)
SK-12	65.88	50	0.307	52	2	-8.82	-7.28	0.691 (0.009)	24.9 (3.3)	-5.0 (0.66)
SK-13	65.92	70	0.311	72	2	-8.17	-8.39	0.693 (0.009)	24.2 (3.2)	-6.2 (0.66)
SK-16	65.98	30	0.316	31	3	-7.16	-7.97	0.703 (0.009)	21.0 (3.1)	-6.5 (0.65)
SK-17	66.60	30	0.366	31	3	-6.57	-11.92	0.682 (0.008)	28.1 (2.8)	-9.0 (0.55)
SK-20	68.61	70	0.478	73	2	-7.60	-9.31	0.688 (0.009)	26.0 (3.3)	-6.8 (0.66)
SK-21	68.61	50	0.478	52	3	-7.52	-9.27	0.710 (0.033)	18.6 (10.6)	-8.3 (2.22)
SK-22	68.62	50	0.479	52	2	-6.80	-9.26	0.695 (0.009)	23.4 (3.2)	-7.3 (0.66)
SK-24	67.24	50	0.403	52	2	-7.37	-9.58	0.716 (0.009)	16.7 (3.0)	-9.0 (0.64)
SK-25	67.39	10	0.411	10	2	-6.78	-11.72	0.676 (0.009)	30.1 (3.4)	-8.4 (0.67)
SK-26	68.87	60	0.498	63	3	-6.39	-8.02	0.693 (0.014)	24.2 (4.9)	-5.9 (1.00)
SK-27	68.93	70	0.503	74	2	-6.43	-8.26	0.690 (0.009)	25.2 (3.3)	-5.9 (0.66)
SK-28	71.05	100	0.668	107	2	-5.06	-11.95	0.699 (0.009)	22.3 (3.2)	-10.2 (0.65)
SK-29	71.43	60	0.699	64	3	-7.87	-11.65	0.666 (0.008)	34.0 (3.0)	-7.6 (0.56)
SK-32	66.22	70	0.336	72	2	-8.83	-9.48	0.683 (0.009)	27.7 (3.4)	-6.6 (0.67)
SK-34	66.26	80	0.339	83	2	-8.25	-8.97	0.681 (0.009)	28.5 (3.4)	-5.9 (0.67)

SK-35	66.31	30	0.343	31	2	-7.36	-11.68	0.686 (0.012)	26.6 (4.2)	-9.0 (0.83)
SK-42	68.00	35	0.445	37	2	-6.64	-9.50	0.676 (0.009)	30.3 (3.5)	-6.1 (0.67)
SK-43	68.12	40	0.451	42	2	-6.53	-8.48	0.709 (0.009)	19.0 (3.1)	-7.4 (0.65)
SK-45	68.45	50	0.466	52	2	-6.62	-8.64	0.691 (0.009)	24.9 (3.3)	-6.3 (0.66)
SK-46	68.50	80	0.471	84	2	-6.66	-8.53	0.703 (0.009)	20.9 (3.1)	-7.1 (0.65)
SK-51	69.39	50	0.539	53	2	-7.79	-11.71	0.695 (0.009)	23.4 (3.2)	-9.7 (0.66)
SK-52	69.64	80	0.558	84	2	-6.37	-10.80	0.691 (0.009)	24.8 (3.3)	-8.5 (0.66)
SK-53	69.88	50	0.577	53	2	-5.83	-13.11	0.685 (0.014)	27.1 (4.8)	-10.4 (0.96)
SK-54	70.08	35	0.594	37	2	-6.59	-13.83	0.680 (0.009)	28.6 (3.4)	-10.8 (0.67)
SK-55	70.36	40	0.627	43	3	-7.05	-12.94	0.679 (0.011)	29.0 (4.1)	-9.8 (0.80)
SK-56	66.92	30	0.387	31	2	-7.15	-11.19	0.706 (0.010)	19.9 (3.4)	-9.9 (0.72)
SKnew-01	65.69	70	0.287	72	2	-8.69	-7.93	0.695 (0.009)	23.6 (3.2)	-5.9 (0.66)
SKknew-05	66.11	30	0.327	31	3	-6.60	-7.17	0.721 (0.008)	15.2 (2.5)	-6.9 (0.53)
SKnew-06-01	66.39	50	0.349	52	3	-6.40	-8.50	0.693 (0.009)	24.2 (3.1)	-6.3 (0.62)
SKnew-06-02	66.39	50	0.349	52	3	-7.10	-9.66	0.696 (0.008)	23.2 (2.7)	-7.7 (0.54)
SKnew-07	66.60	30	0.366	31	3	-5.90	-9.40	0.717 (0.008)	16.4 (2.6)	-8.9 (0.56)
SKnew-08	66.60	30	0.366	31	3	-6.64	-11.60	0.708 (0.008)	19.1 (2.6)	-10.5 (0.55)
SKnew-09	66.78	25	0.380	26	3	-8.38	-10.85	0.712 (0.009)	17.9 (3.1)	-10.0 (0.65)
SKnew-12	69.18	45	0.523	47	2	-7.12	-10.71	0.716 (0.014)	16.8 (4.6)	-10.1 (0.97)
SKnew-13	72.10	50	0.753	54	2	-8.13	-11.35	0.718 (0.009)	16.0 (3.0)	-10.9 (0.64)
SKnew-14	72.28	65	0.765	70	2	-8.06	-9.93	0.704 (0.009)	20.5 (3.1)	-8.5 (0.65)
SKnew-15	72.55	50	0.784	54	2	-6.66	-14.00	0.645 (0.015)	42.1 (6.1)	-8.4 (1.10)
SKnew-16	72.98	45	0.814	49	2	-6.27	-11.43	0.687 (0.009)	26.5 (3.3)	-8.8 (0.66)
SKnew-18	73.83	55	0.861	60	2	-6.84	-9.88	0.676 (0.020)	30.2 (7.1)	-6.5 (1.39)

SKnew-20	74.23	50	0.887	54	2	-6.84	-11.81	0.686 (0.019)	26.7 (6.9)	-9.2 (1.36)
SKnew-21	75.36	45	0.968	49	2	-6.20	-10.25	0.655 (0.009)	38.2 (3.7)	-5.4 (0.69)
SKnew-22	75.77	50	1.001	55	2	-6.66	-10.90	0.669 (0.015)	32.9 (5.6)	-7.0 (1.08)

* Age model see Supplementary text.

† Dp/Ds are the burial/original depths carbonate nodules blew the paleosol surfaces.

‡ Number of unique analyses of CO_2 from carbonate.

§ VPDB = Vienna Pee Dee Belemnite. Uncertainties on $\delta^{13}C$ and $\delta^{18}O$ are < 0.07‰ and 0.06‰ respectively.

¶ ARF = Absolute Reference Frame. With acid correction of 0.082‰. Uncertainty is reported in parentheses. Standard error of Δ47, SE = SD/SQRT (N). When SD of a sample is less than the observed long-term SD of lab standards (0.013‰), the long-term value of 0.013‰ is assigned as the SD of the sample.

‖ Calculated using the Equation (5) in Passey and Henkes (2012). Uncertainty is reported in parentheses.

** VSMOW = Vienna Standard Mean Ocean Water. Calculated using the equation reported in Kim and O'Neil (1997). Uncertainty is reported in parentheses.

Table DR5 A summary of climatic parameters.

Age* (Ma)	Burial depth (km)	$\delta^{13}C$† (‰, VPDB)	$\delta^{18}O$† (‰, VPDB)	T(Δ47)‡ (°C)	$\delta^{18}O_{water}$§ (‰, VSMOW)	pCO_2¶ (ppmv)
65.52	0.269	-8.67	-7.84	22.6 (2.3)	-6.0 (0.46)	1187 (220)
65.69	0.287	-8.69	-7.93	23.6 (3.2)	-5.9 (0.66)	1048 (302)
65.78	0.297	-9.07	-9.15	25.1 (2.3)	-6.8 (0.47)	1180 (217)
65.79	0.298	-8.57	-9.54	30.6 (3.5)	-6.1 (0.67)	1075 (374)
65.81	0.300	-7.99	-8.87	24.6 (2.4)	-6.5 (0.49)	938 (250)
65.82	0.301	-7.07	-8.81	27.2 (3.3)	-6.0 (0.67)	1238 (488)
65.88	0.307	-8.82	-7.28	24.9 (3.3)	-5.0 (0.66)	800 (283)
65.92	0.311	-8.17	-8.39	24.2 (3.2)	-6.2 (0.66)	1251 (352)
65.98	0.316	-7.16	-7.97	21.0 (3.1)	-6.5 (0.65)	806 (381)
66.11	0.327	-6.60	-7.17	15.2 (2.5)	-6.9 (0.53)	701 (329)
66.22	0.336	-8.83	-9.48	27.7 (3.4)	-6.6 (0.67)	1059 (307)
66.26	0.339	-8.25	-8.97	28.5 (3.4)	-5.9 (0.67)	1468 (382)
66.31	0.343	-7.36	-11.68	26.6 (4.2)	-9.0 (0.83)	863 (414)
66.39	0.349	-6.75	-9.08	22.6 (2.0)	-7.1 (0.41)	1285 (308)
66.60	0.366	-6.37	-10.97	20.9 (1.5)	-9.5 (0.32)	870 (237)
66.78	0.380	-8.38	-10.85	17.9 (3.1)	-10.0 (0.65)	348 (189)
66.92	0.387	-7.15	-11.19	19.9 (3.4)	-9.9 (0.72)	665 (317)
67.24	0.403	-7.37	-9.58	16.7 (3.0)	-9.0 (0.64)	806 (281)
67.39	0.411	-6.78	-11.72	30.1 (3.4)	-8.4 (0.67)	587 (476)
68.00	0.445	-6.64	-9.50	30.3 (3.5)	-6.1 (0.67)	1228 (523)
68.12	0.451	-6.53	-8.48	19.0 (3.1)	-7.4 (0.65)	987 (387)
68.45	0.466	-6.62	-8.64	24.9 (3.3)	-6.3 (0.66)	1333 (451)
68.50	0.471	-6.66	-8.53	20.9 (3.1)	-7.1 (0.65)	1686 (422)
68.61	0.478	-7.56	-9.29	25.4 (3.2)	-6.9 (0.63)	1132 (286)
68.62	0.479	-6.80	-9.26	23.4 (3.2)	-7.3 (0.66)	1212 (411)
68.87	0.498	-6.39	-8.02	24.2 (4.9)	-5.9 (1.00)	1609 (516)
68.93	0.503	-6.43	-8.26	25.2 (3.3)	-5.9 (0.66)	1850 (499)
69.18	0.523	-7.12	-10.71	16.8 (4.6)	-10.1 (0.97)	813 (316)
69.39	0.539	-7.79	-11.71	23.4 (3.2)	-9.7 (0.66)	894 (309)
69.64	0.558	-6.37	-10.80	24.8 (3.3)	-8.5 (0.66)	2175 (534)
69.88	0.577	-5.83	-13.11	27.1 (4.8)	-10.4 (0.96)	1856 (647)
70.08	0.594	-6.59	-13.83	28.6 (3.4)	-10.8 (0.67)	1264 (532)
70.36	0.627	-7.05	-12.94	29.0 (4.1)	-9.8 (0.80)	1248 (492)
71.05	0.668	-5.06	-11.95	22.3 (3.2)	-10.2 (0.65)	3460 (719)
71.43	0.699	-7.87	-11.65	34.0 (3.0)	-7.6 (0.56)	1553 (454)
72.10	0.753	-8.13	-11.35	16.0 (3.0)	-10.9 (0.64)	680 (237)
72.28	0.765	-8.06	-9.93	20.5 (3.1)	-8.5 (0.65)	992 (291)
72.55	0.784	-6.66	-14.00	42.1 (6.1)	-8.4 (1.10)	2454 (885)
72.98	0.814	-6.27	-11.43	26.5 (3.3)	-8.8 (0.66)	1473 (521)
73.83	0.861	-6.84	-9.88	30.2 (7.1)	-6.5 (1.39)	1660 (609)
74.23	0.887	-6.84	-11.81	26.7 (6.9)	-9.2 (1.36)	1396 (533)

75.36	0.968	-6.20	-10.25	38.2 (3.7)	-5.4 (0.69)	2203 (775)
75.77	1.001	-6.66	-10.90	32.9 (5.6)	-7.0 (1.08)	1738 (616)

* Age model see Supplementary text.

† VPDB = Vienna Pee Dee Belemnite. Uncertainties on $\delta^{13}C$ and $\delta^{18}O$ are < 0.07‰ and 0.06‰ respectively.

‡ Calculated using the Equation (5) in Passey and Henkes (2012). Uncertainty is reported in parentheses.

§ VSMOW = Vienna Standard Mean Ocean Water. Calculated using the equation reported in Kim and O'Neil (1997). Uncertainty is reported in parentheses.

¶ Calculated using the equations of Breecker and Retallack (2014). Uncertainty is reported in parentheses.